

Article

The Electrocatalytic Oxygen Evolution Reaction Activity of Rationally Designed NiFe-Based Glycerates

Vivek Kumar Singh [†], Bibhudatta Malik [†], Rajashree Konar , Efrat Shawat Avraham and Gilbert Daniel Nessim ^{*†} 

Department of Chemistry, Bar Ilan Institute for Nanotechnology and Advanced Materials (BINA), Bar Ilan University, Ramat Gan 52900, Israel; vivekkumarsingh.rs.cer18@itbhu.ac.in (V.K.S.); malikbi@biu.ac.il (B.M.); rajashree.konar@biu.ac.il (R.K.); epale086@gmail.com (E.S.A.)

* Correspondence: gdnessim@biu.ac.il

[†] These authors contributed equally to this work.

Abstract: The electrocatalytic oxygen evolution reaction (OER) is an arduous step in water splitting due to its slow reaction rate and large overpotential. Herein, we synthesized glycerate-anion-intercalated nickel–iron glycerates (NiFeGs) using a one-step solvothermal reaction. We designed various NiFeGs by tuning the molar ratio between Ni and Fe to obtain Ni₄Fe₁G, Ni₃Fe₁G, Ni₃Fe₂G, and Ni₁Fe₁G, which we tested for their OER performance. We initially analyzed the catalytic performance of powder samples immobilized on glassy carbon electrodes using a binder. Ni₃Fe₂G outperformed the other NiFeG compositions, including NiFe layered double hydroxide (LDH). It exhibited an overpotential of 320 mV at a current density of 10 mA cm⁻² in an electrolytic solution of pH 14. We then synthesized carbon paper (CP)-modified Ni₃Fe₂G as a self-supported electrode (Ni₃Fe₂G/CP), and it exhibited a high current density (100 mA cm⁻²) at a low overpotential of 300 mV. The redox peak analysis for the NiFeGs revealed that the initial step of the OER is the formation of γ -NiOOH, which was further confirmed by a post-Raman analysis. We extensively analyzed the catalyst's stability and lifetime, the nature of the active sites, and the role of the Fe content to enhance the OER performance. This work may provide the motivation to study metal-alkoxide-based efficient OER electrocatalysts that can be used for alkaline water electrolyzer applications.

Keywords: oxygen evolution reaction (OER); nickel–iron glycerate (NiFeG); layered double hydroxide (LDH); overpotential; cyclic voltammograms (CVs)



Citation: Singh, V.K.; Malik, B.; Konar, R.; Avraham, E.S.; Nessim, G.D. The Electrocatalytic Oxygen Evolution Reaction Activity of Rationally Designed NiFe-Based Glycerates. *Electrochem* **2024**, *5*, 70–83. <https://doi.org/10.3390/electrochem5010005>

Received: 24 November 2023

Revised: 15 December 2023

Accepted: 15 January 2024

Published: 4 February 2024



Copyright: © 2024 by the authors. Licensee MDPI, Basel, Switzerland. This article is an open access article distributed under the terms and conditions of the Creative Commons Attribution (CC BY) license (<https://creativecommons.org/licenses/by/4.0/>).

1. Introduction

The oxygen evolution reaction (OER) is a crucial step in the generation of hydrogen in electrochemical water splitting, as well as for rechargeable metal–air batteries for energy conversion [1,2]. The OER is a half-cell anodic reaction of water splitting that is important for energy conversion. However, the OER is very challenging due to the sluggish reaction kinetics, owing to the four-proton-coupled electron transfer process [3]. Precious metal oxides, particularly ruthenium oxide (RuO₂) and iridium oxide (IrO₂), still remain the benchmark catalysts for the OER [4–6]. Unfortunately, their limited availability in the earth's crust and their high cost hinder their widespread use. Additional issues with RuO₂ and IrO₂ restrict their practical use such as RuO₂ producing RuO₄²⁻ and dissolving at a high positive potential during the OER, thus limiting its durability [7,8]. Therefore, we seek highly active, low-cost, earth-abundant, and highly stable OER electrocatalysts to eliminate the overpotential associated with the slow kinetics of multistep proton-coupled electron transfer processes.

Utilizing earth-abundant non-precious metal-based catalysts, such as transition metal oxides, hydroxides (M-(OH)_y), layered double hydroxides (LDH; M-O_x(OH)_y), chalcogenides, and pnictides, is attracting a lot of attention [9–14]. First-row transition metal hydroxides/(oxy) hydroxides, which include both Ni and Fe, are the most effective and

promising catalysts for the OER in alkaline media. These catalysts exhibit a much greater activity compared to those that only contain Fe or Ni [15–18]. Numerous investigations have revealed that the presence of Fe as a synergistic component enhances the OER activity of NiFe oxyhydroxides. This component not only induces a partial charge transfer to activate Ni-surrounded centers but also provides catalytic systems with an improved charge-carrier density [2]. Unfortunately, the OER electrocatalytic reaction performance of Ni- or Fe-based hydroxides or (oxy)hydroxides is limited by their low conductivity due to easy aggregation, narrow electrochemical surface area (ECSA), and inability to meet practical applications [19]. It is therefore important to develop or modify the existing NiFe-based catalysts with a structure identical to Fe/Ni oxides/(oxy)hydroxides, which is optimal for the OER.

Recently, transition-metal-based alkoxides, mainly glycerates, were developed as a new class of OER electrocatalysts owing to their structure. Metal glycerates have a layered structure consisting of intercalated glycerate anions between stacked metal–oxygen sheets [20–22]. The layered structure looks similar to anion-intercalated hydroxides, which offers an ideal interlayer spacing for reactant accommodation [23]. Furthermore, during the OER, the preferred OOH functional group forms because of its resemblance to the hydroxide. Wang et al. reported that bimetallic FeNi-glycerate microspheres exhibited a 12 h long-term stability and an overpotential of 320 mV at a 10 mA cm⁻² current density in a 1M KOH aqueous solution. The strong electronic interaction between Fe and Ni in FeNi-glycerates and their unique structures are responsible for their enhanced OER performance [23]. Dong et al. reported that CoFe glycerate hollow spheres exhibited an overpotential of 242 mV at a 10 mA cm⁻² current density, a narrow Tafel slope (49.4 mV/dec), and a high stability in alkaline conditions [24]. Although Wang et al. studied the OER performance of Fe_xNi_{1-x} glycerolate, the nature of the active species responsible for the OER and the critical role of the Fe amount in enhancing the OER are still not understood.

Can we improve the performance of NiFeG to approach or surpass that of RuO₂ or IrO₂? Inspired by the unique structural chemistry and OER performance of metal alkoxides, we rationally prepared various NiFeG-based electrocatalysts and studied their OER electrocatalytic properties. With the help of surface redox chemistry and exsitu Raman studies, we elucidate the active species for the OER. Researchers have found that the enhanced OER activity of Ni(OH)₂ could be achieved by tuning the Fe content between 20% and 30% [25]. In the present study, we demonstrate that NiFeG with a composition of Ni (60%)/Fe (40%) exhibited the maximum OER performance. However, the performance started to decline upon the further increase in the Fe concentration. This research shows there is an opportunity to reduce the Ni content in OER electrocatalysts by using Ni-based alkoxide-type catalysts.

2. Synthesis of Nickel–Iron Glycerate (NiFeG) Microspheres

Nickel–iron glycerate (NiFeG) microspheres were synthesized using a one-pot solvothermal process. In a typical procedure, iron (III) nitrate nonahydrate (Fe(NO₃)₃·9H₂O, 98%) and nickel (II) nitrate hexahydrate (Ni(NO₃)₂·6H₂O, 98%) were dissolved in a mixed solution containing 8 mL of glycerol (HOCH₂CH(OH)CH₂OH, 99%) and 24 mL of isopropyl alcohol (IPA, 99.5%), which was followed by stirring the solution for 30 min at 500 rpm to obtain a homogeneous solution. The homogenous solution was then placed in a 50 mL Teflon-lined autoclave and heated to 180 °C for 15 h. The Teflon autoclave spontaneously cooled to ambient temperature after the reaction period. Finally, the NiFe-glycerate (NiFeG) microspheres were separated via centrifugation, washed three times with deionized water (DI) and absolute ethanol, and dried at 80 °C for 12 h. Different nickel–iron glycerate samples were also synthesized using a similar process by changing the molar ratios of nickel (Ni) and iron (Fe). The Ni-to-Fe ratio had a specific molar ratio of 1:1 when preparing Ni₁Fe₁, 3:2 for Ni₃Fe₂, 3:1 for Ni₃Fe₁, and 4:1 for Ni₄Fe₁. Ni₃Fe₂G on carbon paper (CP, TGP-H-60, Thermo scientific, Waltham, MA, USA) was synthesized using a similar method;

we used $2 \times 2 \text{ cm}^2$ of Toray carbon paper for the growth of NiFeG. We describe the detailed synthesis procedure of Ni_3Fe_1 LDH in the supporting information.

3. Result and Discussion

The phase and crystal structure of the synthesized nickel–iron LDH and glycerates (NiFeG) were examined by X-ray diffraction (XRD). Figure 1a shows the XRD diffraction pattern of the NiFe LDH (black), with the diffraction peaks observed at 11.7° , 23.59° , 34.54° , 39.10° , 46.71° , 60.12° , and 61.33° corresponding to the (003), (006), (012), (015), (018), (011), and (113) of a typical NiFe-based layered structure. The XRD pattern matches well with the reference card (JCPDS 40-0216) [15]. The NiFeG samples exhibited characteristic diffraction peaks at 11.34° , 18.83° , 34.50° , and 60.86° , with these diffraction peaks being attributed to the metal-glycerolate phase and in good agreement with those of the metal-alkoxides commonly produced in glycerol, which is composed of stacked metal-oxygen sheets separated by bonded glycerate ions [21,24]. The corresponding d -spacing of the (003) plane was found to be 7.86 \AA , as calculated using Bragg's equation. The absence of any further peak in the XRD pattern suggests that NiFeG was successfully synthesized using a solvothermal process. Fourier transform infrared spectroscopy (FTIR) was used to further investigate the molecular structure of the as-synthesized NiFe LDH and NiFeG samples. The FTIR spectrum of the NiFe LDH is displayed in Figure S1 (SI), where the large bands centered at $\sim 3398 \text{ cm}^{-1}$ and $\sim 1652 \text{ cm}^{-1}$ were derived from the stretching and bending modes of the O–H groups. The stretching vibration of the CO_3^{2-} anions was observed at $\sim 1355 \text{ cm}^{-1}$ due to the decomposition of urea during the LDH synthesis. The bands observed at $\sim 770 \text{ cm}^{-1}$ may be ascribed to the vibrations of metal–oxygen bonds (M–O, M–O–M, and M–OH) in the LDH [26]. All the NiFeG samples showed the same spectrum because of their inherent glycerol moieties (Figure 1b). The stretching vibrations of hydrogen-bonded O–H groups were responsible for the wide absorption band at $\sim 3350 \text{ cm}^{-1}$, while the two small absorption bands at ~ 2877 and $\sim 2942 \text{ cm}^{-1}$ were assigned to the C–H stretching vibrations due to the presence of organic glycerol ($\text{OHCH}_2\text{-CHOH-CH}_2\text{OH}$) in the NiFeG [21]. At $\sim 1602 \text{ cm}^{-1}$, the high intensity band was associated with the C=C stretching vibration [27]. The absorption band at $\sim 1359 \text{ cm}^{-1}$ was associated with the C–H bending vibration, whereas the band at $\sim 1112 \text{ cm}^{-1}$ was attributed to the stretching vibration of C–O [22]. The out-of-plane C–H bending vibrations were responsible for the peak at $\sim 799 \text{ cm}^{-1}$ [21]. Furthermore, the presence of metal–oxygen (Ni–O, Fe–O, and M) in the NiFe–glycerate stretching vibrations was linked to another notable infrared band, which was centered at a distance between ~ 670 and $\sim 602 \text{ cm}^{-1}$ [23]. In conclusion, FTIR and XRD confirmed the bimetallic glycerates.

We used scanning electron microscopy (SEM) and transmission electron microscopy (TEM) to check the morphology and structure of the NiFe-glycerate (NiFeG) samples. The SEM images of $\text{Ni}_1\text{Fe}_1\text{G}$ showed a uniformly dispersed and rough surface of the solid spherical structures with an average diameter of $\text{Ni}_1\text{Fe}_1\text{G}$ estimated around 4.36 \mu m (Figure S2a,b (SI)). When further increasing the Ni amount in the $\text{Ni}_3\text{Fe}_2\text{G}$ sample, we noticed two kinds of microspheres: a rough solid spherical structure and spheres exhibiting a unique three-dimensional (3D) hierarchical architecture consisting of many two-dimensional (2D) nanosheets perpendicular to the surface of the spheres, with an average microsphere diameter of around 2.78 \mu m (Figure 2a,b). All the nanosheets were interweaved and interlaced like petals to generate a unique 3D open structure with numerous voids and channels that could permit electrolyte access throughout the electrocatalytic process. Further increasing the Ni amount to $\text{Ni}_3\text{Fe}_1\text{G}$ and $\text{Ni}_4\text{Fe}_1\text{G}$ showed a uniformly dispersed and rough surface solid spherical structure similar to the $\text{Ni}_1\text{Fe}_1\text{G}$ sample, as shown in Figure S2c–f (SI). For all the NiFeG samples, the coexistence of nickel, iron, oxygen, and carbon elements in the SEM-EDS images is shown in Figure S3. The ratios of Ni to Fe (Table S1) were 1:1, 3:2, 3:1, and 4:1 in the $\text{Ni}_1\text{Fe}_1\text{G}$, $\text{Ni}_3\text{Fe}_2\text{G}$, $\text{Ni}_3\text{Fe}_1\text{G}$, and $\text{Ni}_4\text{Fe}_1\text{G}$, respectively. Figure S4 shows the SEM images of the NiFe LDH sample, which also shows the ultrathin two-dimensional (2D) nanosheet-like structure with sharp edges. The transmis-

sion electron microscopy (TEM) images confirmed the hierarchical microsphere assembled by the two-dimensional (2D) nanosheets feature of the synthesized $\text{Ni}_3\text{Fe}_2\text{G}$ sample, as shown in Figure 2c, which is consistent with the SEM observations. The 2D-nanosheet-assembled microspheres with a rough surface can be clearly observed in the magnified images shown in Figure 2d. HRTEM and SAED (inserts in Figure 2d) showed the formation of an amorphous and crystalline structure with a d -spacing of 0.26 nm (Figure 2d(inserts) yellow square), which is related to the (012) facet of hexagonal NiFe bimetallic glycerates (JCPDS 40-0216). As seen in Figure 2e,f, dark-field scanning transmission electron microscopy (STEM) combined with energy-dispersive X-ray spectroscopy (STEM-EDS) maps of the NiFeG revealed that the nickel, iron, oxygen, and carbon elements were uniformly distributed throughout the microspheres. According to the EDS results (Figure S5), the distribution of the different elements in atomic percentages (Table S2) was Ni (18.43%), Fe (25.65%), and O (55.92%), respectively.

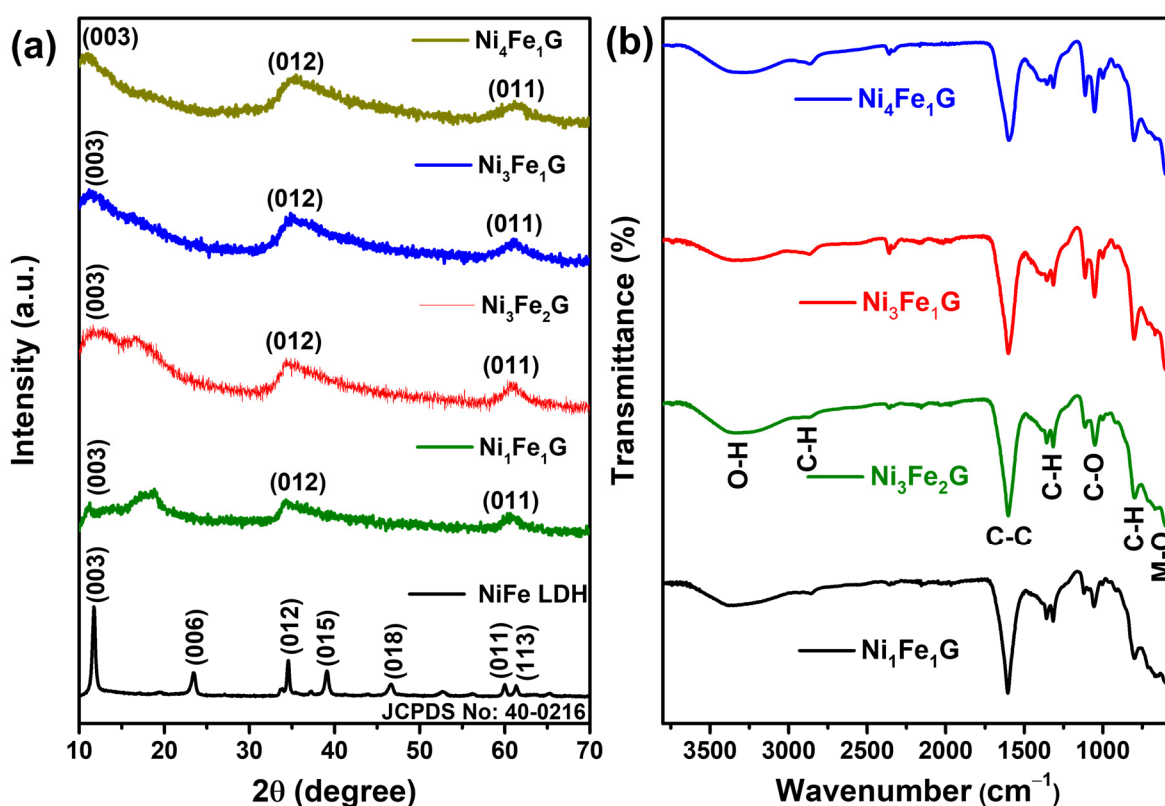


Figure 1. (a) Comparative XRD pattern of various as-synthesized NiFe LDH and NiFeG microspheres; (b) Fourier transform infrared (FTIR) spectrum of as-synthesized NiFe-glycerate samples.

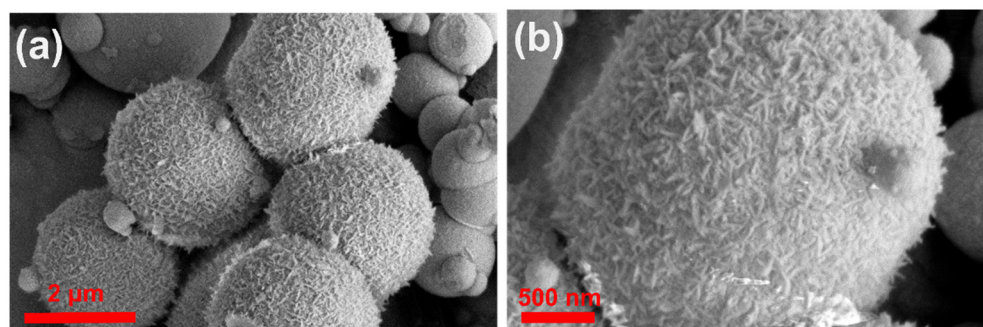


Figure 2. Cont.

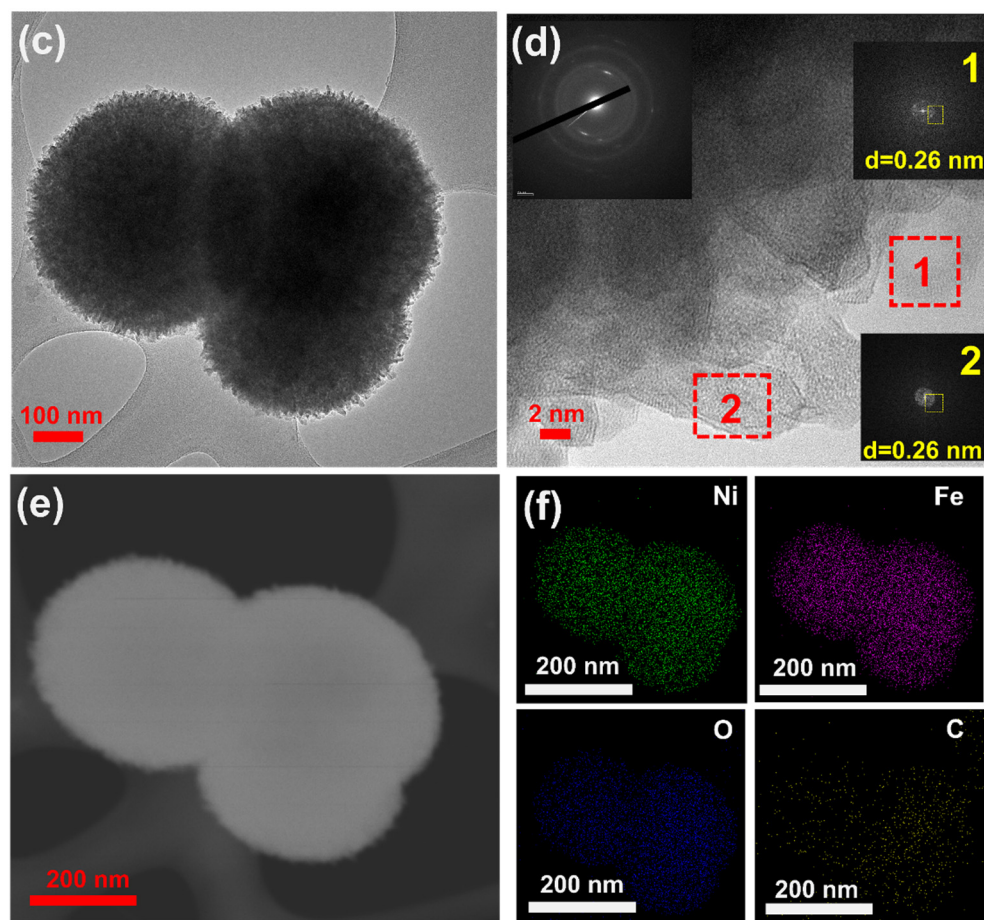


Figure 2. (a,b) SEM images of $\text{Ni}_3\text{Fe}_2\text{G}$ microsphere with different magnifications; (c) TEM images show the uniform size of $\text{Ni}_3\text{Fe}_2\text{G}$ microsphere; (d) HRTEM with SAED (inserts); (e) HAADF-STEM image; and (f) STEM EDS mapping of $\text{Ni}_3\text{Fe}_2\text{G}$ microsphere.

The chemical composition and oxidation states of the as-synthesized NiFeG (Ni_3Fe_2) sample were further investigated using X-ray photoelectron spectroscopy (XPS). The survey spectrum (Figure S6) of the NiFeG clearly showed the existence of Ni, Fe, C, and O elements without other impurity peaks. The XPS spectrum of Ni 2p deconvoluted into the four peaks, as shown in Figure 3a. The fitting peaks located at ~ 855.78 and ~ 873.68 eV corresponded to the Ni $2p_{3/2}$ (Ni^{2+}) and Ni $2p_{1/2}$ (Ni^{2+}), respectively [28]. The other two nickel satellite peaks were also observed at ~ 861.58 and ~ 879.78 eV, respectively [29]. The high-resolution Fe 2p spectrum (Figure 3b) displayed widened Fe $2p_{3/2}$ and Fe $2p_{1/2}$ peaks, trivalent iron (Fe^{3+}) located at ~ 712.67 and ~ 724.45 eV, respectively, and another peak at ~ 710.25 eV that was attributed to the Fe-O bond [30]. The XPS spectrum of O 1s was deconvoluted into four peaks (Figure 3c), where the peak at lower binding energy (~ 530.28 eV) was attributed to the metal-oxygen (M-O) band, while the other peaks located at ~ 531.33 , ~ 532 , and ~ 533.2 eV were attributed to the lattice oxygen related with metal-hydroxide (M-OH), C-O bonding, and surface-absorbed water, respectively [21]. As shown in Figure 3d, the high-resolution C 1s spectrum was deconvoluted into four distinct peaks. The peaks at ~ 284.54 , ~ 285.83 , ~ 287.36 , and ~ 288.26 eV were attributed to the C-C, C-O, C=O, and O=C-O bonding from the carboxyl groups that are present in glycerol, respectively [25].

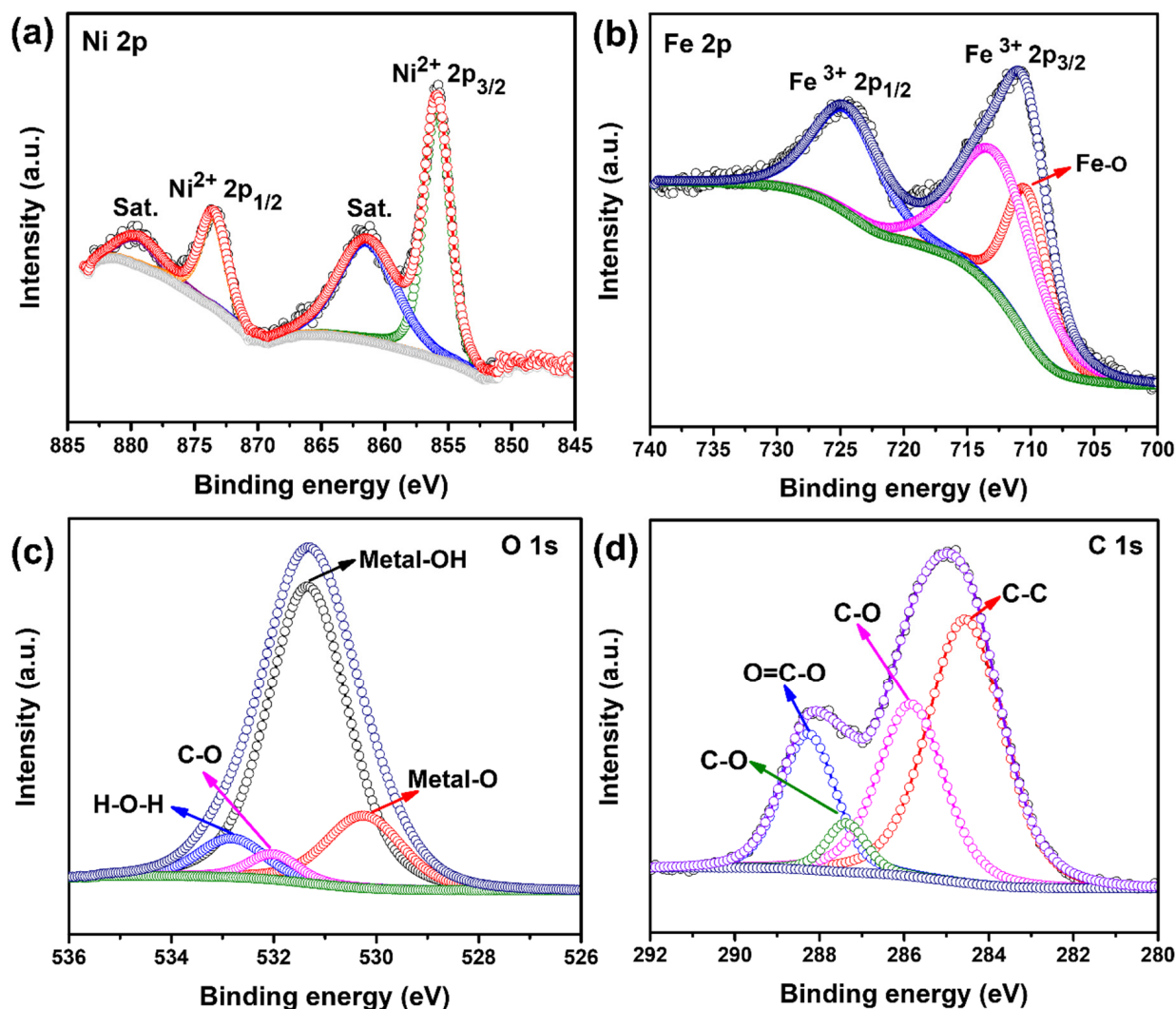


Figure 3. (a) Ni 2p; (b) Fe 2p; (c) O 1s; and (d) C 1s high-resolution XPS spectra of as-synthesized $\text{Ni}_3\text{Fe}_2\text{G}$ microspheres.

4. Electrocatalytic OER Results and Discussions

We tested our materials for their OER activity in 1M KOH (pH 14) using a three-electrode set-up with a glassy carbon electrode (GCE) with our modified catalysts as the working electrode, a platinum counter electrode, and Hg/HgO as a reference electrode. Cyclic voltammograms (CVs) of the synthesized NiFeG catalysts showed the different current responses and their correlation with the Faradic processes (Figure 4). The $I-V$ curves of all the catalysts demonstrated non-Faradic and Faradic processes, which are the combination of metal oxidations followed by O_2 evolution. Each NiFeG catalyst exhibited two types of redox, such as a first oxidation (A1), a first reduction (C2), a second oxidation (A2), and a second reduction (C2) (inset of each plot in Figure 4). In all four cases, we observed the peaks of the redox couple A1/C2 at 1.42 V/1.35 vs. RHE, which was due to the transformations of Ni(II) to Ni(III) and of Ni(III) to $\beta\text{-NiOOH}$. We observed further transformations to higher oxidation states of Ni(III) to $\text{Ni}^{3+\delta}$ ($\delta = 0.5-1$). Anodic waves (A2) at potentials greater than 1.45 V vs. RHE. $\text{Ni}^{3+\delta}$ could be related to the γ phase of NiOOH ($\gamma\text{-NiOOH}$), where the average oxidation state of Ni is 3.67 or higher [31,32].

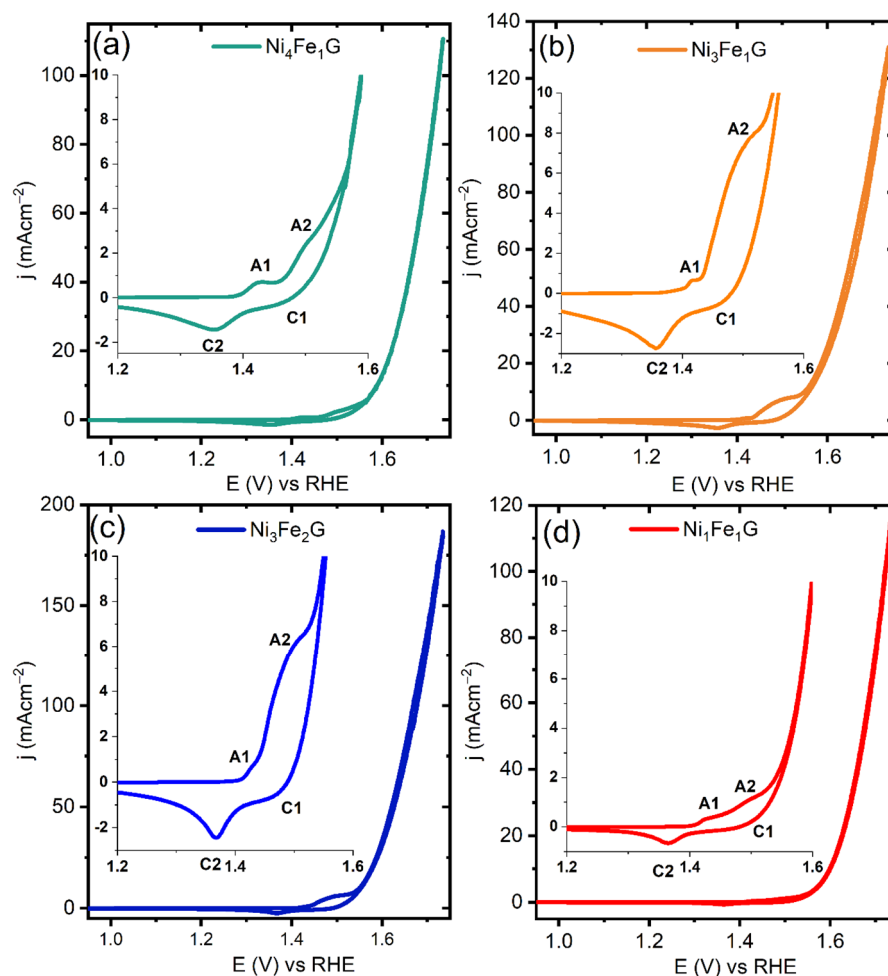


Figure 4. Cyclic voltammograms (CVs) of NiFe glycerates carried out at scan rate of 20 mVs^{-1} , where the insets present the magnified image of the corresponding plots for better visualization: (a) $\text{Ni}_4\text{Fe}_1\text{G}$; (b) $\text{Ni}_3\text{Fe}_1\text{G}$; (c) $\text{Ni}_3\text{Fe}_2\text{G}$; and (d) $\text{Ni}_1\text{Fe}_1\text{G}$.

The reduction regions of the CVs unveiled two peaks (C1 and C2) that were assigned to the reduction of $\gamma\text{-NiOOH} \rightarrow \beta\text{-NiOOH} \rightarrow \beta\text{-Ni(OH)}_2$. As per previous reports, the presence of double reduction peaks for Ni-based systems (at high and low potentials) can be attributed to the reduction of both $\gamma\text{-NiOOH}$ and $\beta\text{-NiOOH}$ to $\beta\text{-Ni(OH)}_2$ [33]. Notably, the redox peak analysis suggests that the OER activity proceeded via the formation of $\gamma\text{-NiOOH}$. The redox peak analysis for the Ni_3Fe_1 LDH showed one redox pair ($\text{Ni}^{2+} \leftrightarrow \text{Ni}^{3+}$), where the active species for OER could be $\beta\text{-NiOOH}$ (Figure S7a) [34].

The linear sweep voltammetry (LSV) polarization results showed that the $\text{Ni}_3\text{Fe}_2\text{G}$ exhibited the lowest OER onset overpotential of 280 mV, while the $\text{Ni}_4\text{Fe}_1\text{G}$, $\text{Ni}_3\text{Fe}_1\text{G}$, and $\text{Ni}_1\text{Fe}_1\text{G}$ exhibited an onset overpotential of 300, 300, and 310 mV, respectively (Figure 5a). The $\text{Ni}_4\text{Fe}_1\text{G}$, $\text{Ni}_3\text{Fe}_1\text{G}$, $\text{Ni}_3\text{Fe}_2\text{G}$, and $\text{Ni}_1\text{Fe}_1\text{G}$ supplied a benchmarking current density (j) of 10 mA cm^{-2} at η values of 360, 340, 320, and 360 mV, respectively. The Tafel slope is an indicator in the kinetics analysis of the OER that is derived from the Tafel equation, $\eta = a + b \log(j)$ (a and b are constants, and j is the current density). The $\text{Ni}_3\text{Fe}_2\text{G}$ had the smallest Tafel slope of 74 mVdec^{-1} , indicating better kinetics than the $\text{Ni}_4\text{Fe}_1\text{G}$, $\text{Ni}_3\text{Fe}_1\text{G}$, and $\text{Ni}_1\text{Fe}_1\text{G}$, whose Tafel slope values were 107, 86, and 96 mVdec^{-1} , respectively (Figure 5b). For comparison, we assessed the OER catalytic performance of Ni and Fe glycerates. The Ni glycerate reached 10 mA cm^{-2} at an η value of 440 mV, while the Fe glycerate showed a very poor catalytic activity, which failed to achieve the benchmarking current density within the studied potential range (Figure S13a). The corresponding Tafel slopes of 115 and

119 mVdec⁻¹ for the Ni and Fe glycerates indicate the sluggish kinetics exhibited by these two catalysts (Figure S13b).

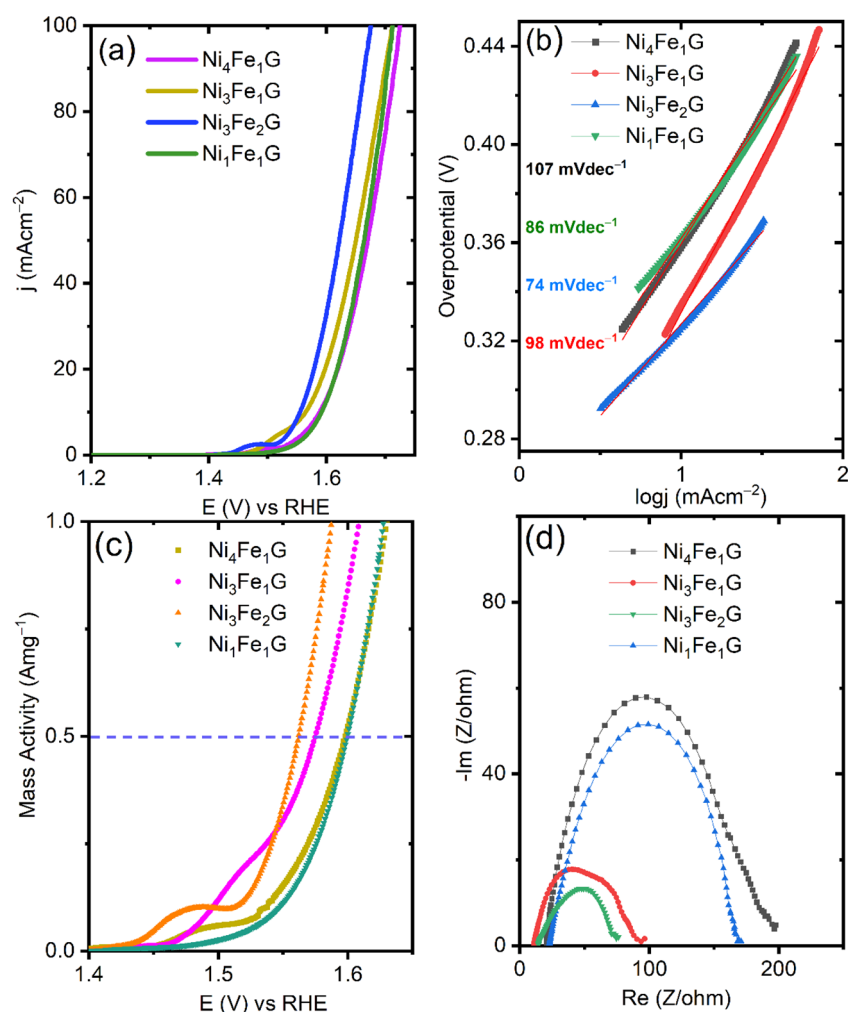


Figure 5. (a) iR-corrected LSV curves of four samples carried out at 5 mVs⁻¹; (b) corresponding Tafel slopes for kinetics determination; (c) mass activity plot of the catalysts, where the dashed line corresponds to the achieved mass activity of 0.5 Amg⁻¹ for each catalyst and; (d) EIS spectra that were taken at 1.55 V vs. RHE for all samples.

As shown in Figure 5c, the Ni₃Fe₂G exhibited an enhanced mass activity of 0.5 Amg⁻¹ at an overpotential of 320 mV, while to reach the same mass activity, the Ni₄Fe₁G, Ni₃Fe₁G, and Ni₁Fe₁G required overpotentials of 340, 360, and 360 mV, respectively. We performed electrochemical impedance spectroscopy (EIS) to assess the mechanism and kinetics of the processes that occurred due to O₂ evolution. The EIS for all the samples was analyzed in the range of 100 kHz–1 mHz (applied amplitude of 10 mV) at a potential of 1.55 V vs. RHE. The NiFeG-based catalysts showed depressed semicircles, indicating a charge transfer process with the absence of diffusion (Figure 5d). Among all, the Ni₃Fe₂G exhibited the smallest arc, which was attributed to its improved electronic conductivity. The fitting parameters for Ni₃Fe₂G are provided in Figure S8 (SI). There were three resistances: solution resistance, bulk resistance, and charge transfer resistance. We compared the OER performance of the NiFeG with the well-studied NiFe LDH (Figure S7b (SI)). The catalytic performance of the Ni₃Fe₁G and NiFe LDH were compared to ensure consistency in the ratios between Ni and Fe. The Ni₃Fe₁ LDH delivered a value of *j* of 10 mA cm⁻² at an η value of 370 mV, which was 30 mV greater than that of Ni₃Fe₁G (Figure S7b), thus revealing the superiority of the NiFe glycerate over NiFe layered double hydroxide.

A chronoamperometric aging test for the $\text{Ni}_3\text{Fe}_2\text{G}$ was performed at 1.55 V vs. RHE in the rotating disk electrode (RDE) mode at a rotation speed of 1600 rpm to gain knowledge on the catalyst's degradation and its relationship with long-term electrolysis. As can be seen from Figure 6a, the initial j within a few seconds was measured at 11.8 mA cm^{-2} , which gradually decayed to 5.56 mA cm^{-2} over a period of 5 h (the current decay could not be avoided even whilst employing RDE). After an hour, the retention percentage of j was 84.8% and, subsequently, the overall current density dropped to 47.5%. The deterioration of the current could be linked to the accumulation of microscopic gas bubbles (O_2) on the catalyst surface, where the bubbles filled the pores or voids that formed at the catalyst layers (interaction between catalyst and ionomer). Blockage of the active sites of the $\text{Ni}_3\text{Fe}_2\text{G}$, which was mainly caused by the formation of microscopic oxygen bubbles, degraded the performance. Catalyst lifetime can be largely improved by preventing the growth of O_2/H_2 gaseous bubbles.

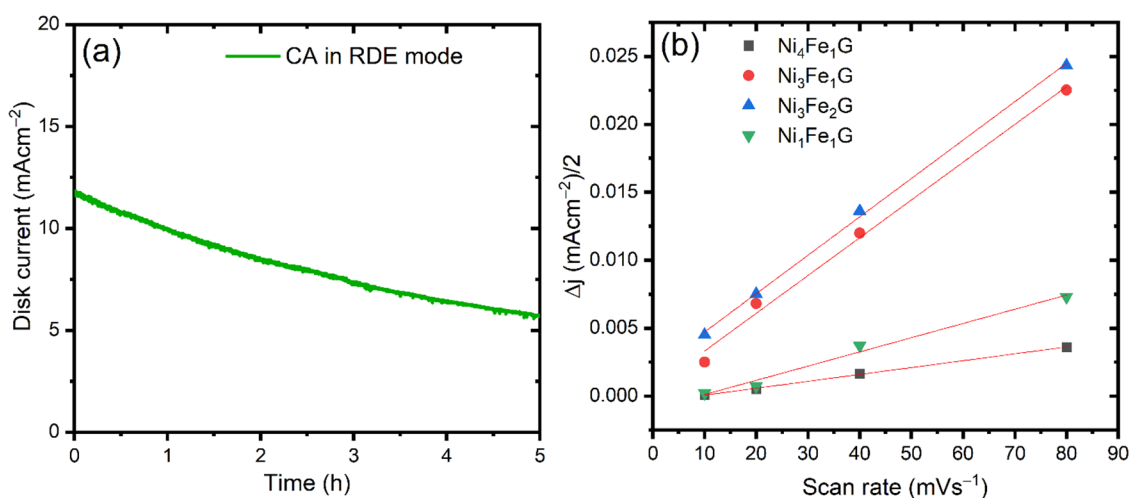


Figure 6. (a) CA test for $\text{Ni}_3\text{Fe}_2\text{G}$ conducted at a rotation speed of 1600 rpm; (b) double-layer capacitance plots of NiFeG catalysts obtained from non-faradic CVs.

We evaluated the double-layer capacitance (C_{dl}) by testing the CVs in the non-Faradic regions for these synthesized catalysts (CVs are given in Figure S9). The C_{dl} values of 0.05, 0.27, 0.29, and 0.1 mF cm^{-2} were assigned to $\text{Ni}_4\text{Fe}_1\text{G}$, $\text{Ni}_3\text{Fe}_1\text{G}$, $\text{Ni}_3\text{Fe}_2\text{G}$, and $\text{Ni}_1\text{Fe}_1\text{G}$, respectively. Then, we calculated the electrochemical active surface area (ECSA) as $\text{ECSA} = [C_{dl}/C_s] \times A$ (C_s represents the capacitance of GCE, and its value is 0.04 mF cm^{-2} , which is the usual C_s value of a planar electrode, and A is the area of the catalyst-modified GCE) [35]. The corresponding ECSAs for the $\text{Ni}_4\text{Fe}_1\text{G}$, $\text{Ni}_3\text{Fe}_1\text{G}$, $\text{Ni}_3\text{Fe}_2\text{G}$, and $\text{Ni}_1\text{Fe}_1\text{G}$ were calculated as 0.0875, 0.4725, 0.5075, and 0.175 cm^2 , respectively. The $\text{Ni}_3\text{Fe}_2\text{G}$ exhibited the highest ECSA among all the other compositions of NiFe glycerates, as shown in Figure 6b.

Inspired by the outstanding OER activity exhibited by the powder $\text{Ni}_3\text{Fe}_2\text{G}$, we grew it over Toray carbon paper (CP) to use it as a self-supported electrode, $\text{Ni}_3\text{Fe}_2\text{G}/\text{CP}$, and to study its OER activity and stability. The X-ray diffraction (XRD) and SEM images along with the energy-dispersive spectroscopy (EDS) results of the $\text{Ni}_3\text{Fe}_2\text{G}$ grown on carbon paper are shown in Figure S10 (SI). Interestingly, the $\text{Ni}_3\text{Fe}_2\text{G}/\text{CP}$ exhibited a low onset overpotential of 260 mV (Figure 7a). Moreover, the $\text{Ni}_3\text{Fe}_2\text{G}/\text{CP}$ yielded high current densities of 50 and 100 mA cm^{-2} at low η values of 270 and 300 mV, respectively. This high activity could be attributed to the intimate contact between the substrate and catalyst, which did not require any binding agent. It also showed a high stability up to 40 h with a negligible current drop, as shown by the chronoamperometry (CA) test (Figure 7b). Remarkably, the retention percentage of j after 40 h of electrolysis was calculated to be 90%. The 10% decay in the current density could be attributed to (a) the concentration of gaseous bubbles on the

electrode surface or (b) catalyst destabilization, which is an inherent property. Comparisons of the OER performance of various non-noble-metal electrocatalysts along with NiFeG are mentioned in Table S3 (SI).

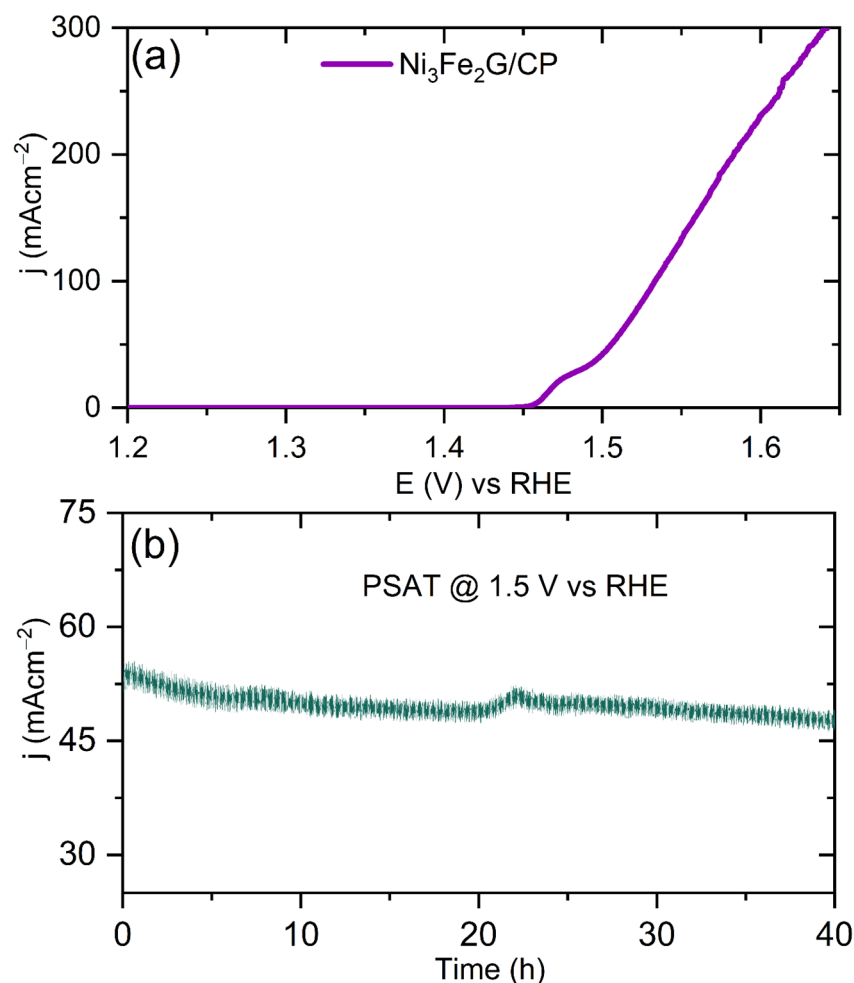


Figure 7. (a) iR-corrected LSV of Ni₃Fe₂G/CP measured at 5 mVs⁻¹; (b) CA test subjected at 1.5 V vs. RHE with the respective j value of 50 mA cm⁻².

Inspired by the outstanding OER activity exhibited by the powder Ni₃Fe₂G, we grew it over Toray carbon paper (CP) to use it as a self-supported electrode, Ni₃Fe₂G/CP, and to study its OER activity and stability. The X-ray diffraction (XRD) and SEM images along with the energy-dispersive spectroscopy (EDS) results of the Ni₃Fe₂G grown on carbon paper are shown in Figure S10 (SI). Interestingly, the Ni₃Fe₂G/CP exhibited a low onset overpotential of 260 mV (Figure 7a). Moreover, the Ni₃Fe₂G/CP yielded high current densities of 50 and 100 mA cm⁻² at low η values of 270 and 300 mV, respectively. This high activity could be attributed to the intimate contact between the substrate and catalyst, which did not require any binding agent. It also showed a high stability up to 40 h with a negligible current drop, as shown by the chronoamperometry (CA) test (Figure 7b). Remarkably, the retention percentage of j after 40 h of electrolysis was calculated to be 90%. The 10% decay in the current density could be attributed to (a) the concentration of gaseous bubbles on the electrode surface or (b) catalyst destabilization, which is an inherent property. Comparisons of the OER performance of various non-noble-metal electrocatalysts along with NiFeG are mentioned in Table S3.

5. Post Characterizations

We carried out a post-XPS analysis of the $\text{Ni}_3\text{Fe}_2\text{G}$ after the 40 h of stability testing to find out the possible changes in the oxidation states of Ni and Fe due to the OER. The Ni 2p spectrum was shifted to a higher binding energy of 1.01 eV and showed a slight broadening (Figure 8a). The XPS spectrum of Ni 2p_{3/2} after the OER showed an additional peak located at 857 eV due to the presence of the Ni^{3+} state (clear indication of the surface reconstruction at the Ni site in the NiFeG). However, after the CA test, the oxidation state of Fe remained unchanged, indicating that the Fe was stable in this structure (Figure 8b). The microstructural changes in the catalyst after the stability test using HR-TEM and SEM are shown in Figure S11 and S12 (SI). We observed, even after 40 h of stability testing, that the $\text{Ni}_3\text{Fe}_2\text{G}$ morphology remained the same. The Raman spectrum of the pristine $\text{Ni}_3\text{Fe}_2\text{G}$ showed peaks positioned at 381.5, 461, and 600 cm^{-1} (Figure 8c). The peak at 381.5 and 600 cm^{-1} could be assigned to the Fe-OH bonding in $\beta\text{-FeOOH}$, where Fe^{3+} ions are octahedrally coordinated [36]. The Raman band at 461 cm^{-1} could be attributed to E_g -type Ni-O vibrations [37]. The Raman spectrum of the post-OER sample showed the retention of the band due to Ni-O vibrations at 461 cm^{-1} ; however, its intensity was reduced significantly compared to the pristine one. After the OER, we observed a new band at 540 cm^{-1} , which was possibly due to the formation of $\gamma\text{-NiOOH}$ [37]. The appearance of another Raman band at 692 cm^{-1} could be assigned to the Fe-O vibrations that exist in amorphous FeOOH [38]. Unambiguously, it can be inferred that the Raman peak at 692 cm^{-1} could be associated with the formation of a new phase of FeOOH other than the β -phase due to the prolonged electrolysis.

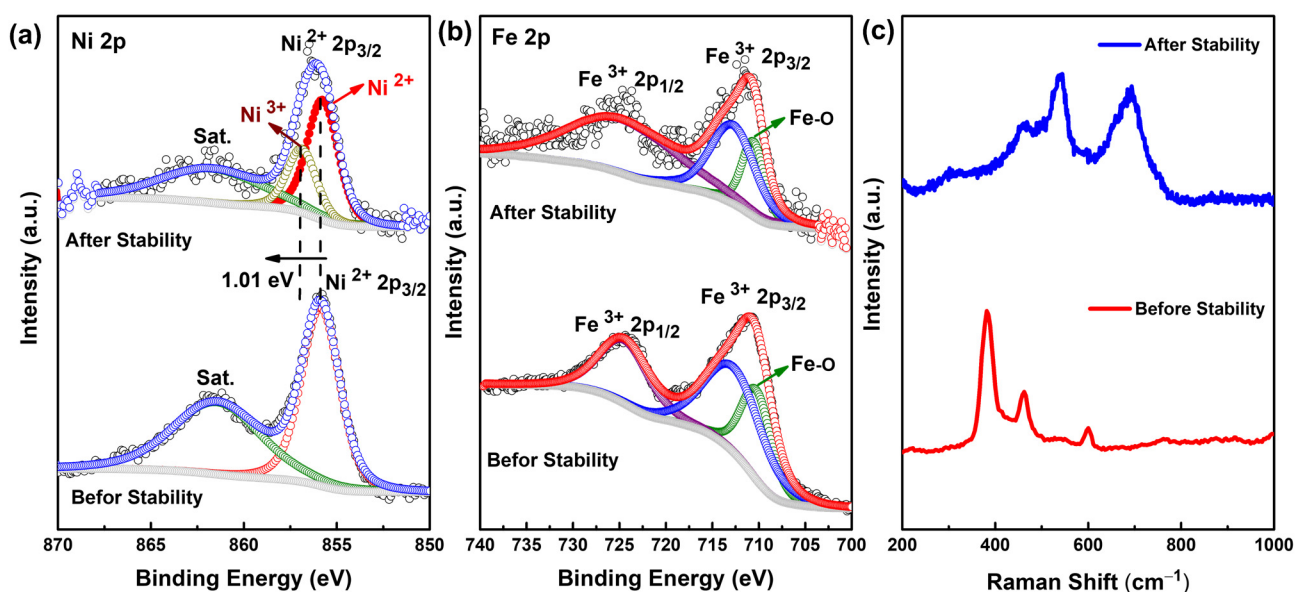


Figure 8. Post-high-resolution XPS results of $\text{Ni}_3\text{Fe}_2\text{G}$: (a) Ni 2p; (b) Fe 2p; and (c) the Raman spectra of $\text{Ni}_3\text{Fe}_2\text{G}$ of both fresh and post-OER samples.

6. Conclusions

In summary, the synthesized $\text{Ni}_3\text{Fe}_2\text{G}$ showed a remarkable OER activity both in powder form and in the self-standing mode on CP. The GCE-modified $\text{Ni}_3\text{Fe}_2\text{G}$ and $\text{Ni}_3\text{Fe}_2\text{G}/\text{CP}$ exhibited low OER onset overpotentials of 280 and 260 mV, respectively. The long-term stability analysis using RDE implied that the decaying of the OER performance was not necessarily due to catalyst poisoning but could be related to the temporary blockage of catalytic active sites due to the formation of micro bubbles or a fractional mass loss of the catalyst due to the failure of the polymeric binder. In contrast, the self-supported $\text{Ni}_3\text{Fe}_2\text{G}/\text{CP}$ demonstrated stability up to 40 h with a 90% retention of j , which was initially recorded as 50 mA cm^{-2} . Redox peak analysis further provided meaningful insights into

the identification of active species in the NiFeG structure. At lower applied potentials, the first oxidation peak (Ni^{2+} to Ni^{3+}) appeared because of the deprotonation that occurred in NiFeG. As the applied potential increased, the Ni^{3+} species further underwent deprotonation to form the higher oxidation state of Ni, γ -NiOOH, which was identified as the true active site. Interestingly, the oxidation state of Fe remained intact even after the OER, as evidenced from the post-XPS analysis. This work will be useful for the exploration of transition-metal-alkoxide-based high-performance electrocatalysts.

Supplementary Materials: The following supporting information can be downloaded at: <https://www.mdpi.com/article/10.3390/electrochem5010005/s1>, Figure S1: FTIR Spectrum of NiFe LDH Sample; Figure S2: SEM images of NiFeG samples (a,b) $\text{Ni}_1\text{Fe}_1\text{G}$; (c,d) $\text{Ni}_3\text{Fe}_1\text{G}$; and (e,f) $\text{Ni}_4\text{Fe}_1\text{G}$; Figure S3: EDS of different ratios of NiFeG sample (1:1, 3:2, 3:1, and 4:1); Table S1: SEM-EDS of the different NiFeG samples; Figure S4: (a,b) FESEM image of the NiFe LDH; Figure S5: TEM EDX of $\text{Ni}_3\text{Fe}_2\text{G}$ sample; Table S2: Elemental distributions of the $\text{Ni}_3\text{Fe}_2\text{G}$ sample; Figure S6: XPS survey of $\text{Ni}_3\text{Fe}_2\text{G}$ sample; Figure S7: (a) OER CV of NiFe LDH; and (b) LSV comparison of $\text{Ni}_3\text{Fe}_1\text{G}$ and $\text{Ni}_3\text{Fe}_1\text{LDH}$; Figure S8: Experimental and fitted EIS spectra of $\text{Ni}_3\text{Fe}_2\text{G}$; Figure S9: CVs with various scan rates for (a) $\text{Ni}_4\text{Fe}_1\text{G}$; (b) $\text{Ni}_3\text{Fe}_1\text{G}$; (c) $\text{Ni}_3\text{Fe}_2\text{G}$; and (d) $\text{Ni}_1\text{Fe}_1\text{G}$; Figure S10: (a) Pristine carbon paper and $\text{Ni}_3\text{Fe}_2\text{G}$ microspheres grown on CP after the solvothermal synthesis; (b) comparative XRD pattern of the CP and $\text{Ni}_3\text{Fe}_2\text{G}/\text{CP}$; (c) SEM images of pristine CP; (d,e) SEM images of $\text{Ni}_3\text{Fe}_2\text{G}$; (f) EDS of $\text{Ni}_3\text{Fe}_2\text{G}$; Figure S11: Structural and morphology characterization of $\text{Ni}_3\text{Fe}_2\text{G}$ sample after the stability test; (a) TEM image, (b) HRTEM image; Figure S12: SEM images of the $\text{Ni}_3\text{Fe}_2\text{G}$ microsphere after the stability test; Figure S13: (a) LSV of Ni and Fe glycerates; and (b) their corresponding Tafel plots; Table S3: Comparison of the OER performance of various non-noble metal electrocatalysts.

Author Contributions: V.K.S. and B.M.: conceptualization, methodology, data curation, validation, investigation, visualization, original draft preparation, and review and editing of the manuscript. R.K. and E.S.A.: formal analysis and software. G.D.N.: review and editing of the manuscript and supervision. All authors have read and agreed to the published version of the manuscript.

Funding: This research received no external funding.

Institutional Review Board Statement: Not applicable.

Informed Consent Statement: Not applicable.

Data Availability Statement: Data are contained within the article and Supplementary Materials.

Acknowledgments: The authors would like to thank the scientists and technicians of the central characterization units of both of the chemistry departments of Bar-Ilan University and Bar-Ilan Institute for Nanotechnology and Advanced Materials (BINA).

Conflicts of Interest: The authors declare no conflicts of interest.

References

1. Jamesh, M.-I.; Sun, X. Recent Progress on Earth Abundant Electrocatalysts for Oxygen Evolution Reaction (OER) in Alkaline Medium to Achieve Efficient Water Splitting—A Review. *J. Power Sources* **2018**, *400*, 31–68. [[CrossRef](#)]
2. Zhao, J.; Zhang, J.; Li, Z.; Bu, X. Recent Progress on NiFe-Based Electrocatalysts for the Oxygen Evolution Reaction. *Small* **2020**, *16*, 2003916. [[CrossRef](#)] [[PubMed](#)]
3. He, Y.; Kang, Z.; Li, J.; Li, Y.; Tian, X. Recent Progress of Manganese Dioxide Based Electrocatalysts for the Oxygen Evolution Reaction. *Ind. Chem. Mater.* **2023**, *1*, 312–331. [[CrossRef](#)]
4. Ying, J.; Chen, J.-B.; Xiao, Y.-X.; Cordoba De Torresi, S.I.; Ozoemena, K.I.; Yang, X.-Y. Recent Advances in Ru-Based Electrocatalysts for Oxygen Evolution Reaction. *J. Mater. Chem. A* **2023**, *11*, 1634–1650. [[CrossRef](#)]
5. Shan, J.; Guo, C.; Zhu, Y.; Chen, S.; Song, L.; Jaroniec, M.; Zheng, Y.; Qiao, S.-Z. Charge-Redistribution-Enhanced Nanocrystalline Ru@IrOx Electrocatalysts for Oxygen Evolution in Acidic Media. *Chem* **2019**, *5*, 445–459. [[CrossRef](#)]
6. Binninger, T.; Doublet, M.-L. The Ir–OOO–Ir Transition State and the Mechanism of the Oxygen Evolution Reaction on IrO₂(110). *Energy Environ. Sci.* **2022**, *15*, 2519–2528. [[CrossRef](#)] [[PubMed](#)]
7. Wang, C.; Jin, L.; Shang, H.; Xu, H.; Shiraiishi, Y.; Du, Y. Advances in Engineering RuO₂ Electrocatalysts towards Oxygen Evolution Reaction. *Chin. Chem. Lett.* **2021**, *32*, 2108–2116. [[CrossRef](#)]
8. Yu, J.; He, Q.; Yang, G.; Zhou, W.; Shao, Z.; Ni, M. Recent Advances and Prospective in Ruthenium-Based Materials for Electrochemical Water Splitting. *ACS Catal.* **2019**, *9*, 9973–10011. [[CrossRef](#)]

9. Trotochaud, L.; Ranney, J.K.; Williams, K.N.; Boettcher, S.W. Solution-Cast Metal Oxide Thin Film Electrocatalysts for Oxygen Evolution. *J. Am. Chem. Soc.* **2012**, *134*, 17253–17261. [[CrossRef](#)]
10. Lu, X.; Xue, H.; Gong, H.; Bai, M.; Tang, D.; Ma, R.; Sasaki, T. 2D Layered Double Hydroxide Nanosheets and Their Derivatives Toward Efficient Oxygen Evolution Reaction. *Nano-Micro Lett.* **2020**, *12*, 86. [[CrossRef](#)]
11. Lim, C.S.; Chua, C.K.; Sofer, Z.; Klímová, K.; Boothroyd, C.; Pumera, M. Layered Transition Metal Oxyhydroxides as Tri-Functional Electrocatalysts. *J. Mater. Chem. A* **2015**, *3*, 11920–11929. [[CrossRef](#)]
12. Ao, K.; Wei, Q.; Daoud, W.A. MOF-Derived Sulfide-Based Electrocatalyst and Scaffold for Boosted Hydrogen Production. *ACS Appl. Mater. Interfaces* **2020**, *12*, 33595–33602. [[CrossRef](#)]
13. Liu, Y.; Guo, Y.; Liu, Y.; Wei, Z.; Wang, K.; Shi, Z. A Mini Review on Transition Metal Chalcogenides for Electrocatalytic Water Splitting: Bridging Material Design and Practical Application. *Energy Fuels* **2023**, *37*, 2608–2630. [[CrossRef](#)]
14. Kawashima, K.; Márquez, R.A.; Smith, L.A.; Vaidyula, R.R.; Carrasco-Jaim, O.A.; Wang, Z.; Son, Y.J.; Cao, C.L.; Mullins, C.B. A Review of Transition Metal Boride, Carbide, Pnictide, and Chalcogenide Water Oxidation Electrocatalysts. *Chem. Rev.* **2023**, *123*, 12795–13208. [[CrossRef](#)]
15. Zhang, J.; Liu, J.; Xi, L.; Yu, Y.; Chen, N.; Sun, S.; Wang, W.; Lange, K.M.; Zhang, B. Single-Atom Au/NiFe Layered Double Hydroxide Electrocatalyst: Probing the Origin of Activity for Oxygen Evolution Reaction. *J. Am. Chem. Soc.* **2018**, *140*, 3876–3879. [[CrossRef](#)]
16. Guo, Y.; Zhang, C.; Zhang, J.; Dastafkan, K.; Wang, K.; Zhao, C.; Shi, Z. Metal–Organic Framework-Derived Bimetallic NiFe Selenide Electrocatalysts with Multiple Phases for Efficient Oxygen Evolution Reaction. *ACS Sustain. Chem. Eng.* **2021**, *9*, 2047–2056. [[CrossRef](#)]
17. Sakamaki, A.; Yoshida-Hirahara, M.; Ogihara, H.; Kurokawa, H. One-Step Synthesis of Highly Active NiFe Electrocatalysts for the Oxygen Evolution Reaction. *Langmuir* **2022**, *38*, 5525–5531. [[CrossRef](#)]
18. Park, K.R.; Jeon, J.; Choi, H.; Lee, J.; Lim, D.-H.; Oh, N.; Han, H.; Ahn, C.; Kim, B.; Mhin, S. NiFe Layered Double Hydroxide Electrocatalysts for an Efficient Oxygen Evolution Reaction. *ACS Appl. Energy Mater.* **2022**, *5*, 8592–8600. [[CrossRef](#)]
19. Han, Q.; Luo, Y.; Li, J.; Du, X.; Sun, S.; Wang, Y.; Liu, G.; Chen, Z. Efficient NiFe-Based Oxygen Evolution Electrocatalysts and Origin of Their Distinct Activity. *Appl. Catal. B Environ.* **2022**, *304*, 120937. [[CrossRef](#)]
20. Larcher, D.; Sudant, G.; Patrice, R.; Tarascon, J.-M. Some Insights on the Use of Polyols-Based Metal Alkoxides Powders as Precursors for Tailored Metal-Oxides Particles. *Chem. Mater.* **2003**, *15*, 3543–3551. [[CrossRef](#)]
21. Nguyen, T.X.; Su, Y.; Lin, C.; Ruan, J.; Ting, J. A New High Entropy Glycerate for High Performance Oxygen Evolution Reaction. *Adv. Sci.* **2021**, *8*, 2002446. [[CrossRef](#)] [[PubMed](#)]
22. Septiani, N.L.W.; Kaneti, Y.V.; Fathoni, K.B.; Guo, Y.; Ide, Y.; Yuliarto, B.; Jiang, X.; Nugraha; Dipojono, H.K.; Golberg, D.; et al. Tailorable Nanoarchitecturing of Bimetallic Nickel–Cobalt Hydrogen Phosphate *via* the Self-Weaving of Nanotubes for Efficient Oxygen Evolution. *J. Mater. Chem. A* **2020**, *8*, 3035–3047. [[CrossRef](#)]
23. Wang, M.; Jiang, J.; Ai, L. Layered Bimetallic Iron–Nickel Alkoxide Microspheres as High-Performance Electrocatalysts for Oxygen Evolution Reaction in Alkaline Media. *ACS Sustain. Chem. Eng.* **2018**, *6*, 6117–6125. [[CrossRef](#)]
24. Dong, Z.; Zhang, W.; Xiao, Y.; Wang, Y.; Luan, C.; Qin, C.; Dong, Y.; Li, M.; Dai, X.; Zhang, X. One-Pot-Synthesized CoFe-Glycerate Hollow Spheres with Rich Oxyhydroxides for Efficient Oxygen Evolution Reaction. *ACS Sustain. Chem. Eng.* **2020**, *8*, 5464–5477. [[CrossRef](#)]
25. Anantharaj, S.; Kundu, S.; Noda, S. “The Fe Effect”: A Review Unveiling the Critical Roles of Fe in Enhancing OER Activity of Ni and Co Based Catalysts. *Nano Energy* **2021**, *80*, 105514. [[CrossRef](#)]
26. Hobbs, C.; Jaskaniec, S.; McCarthy, E.K.; Downing, C.; Opelt, K.; Güth, K.; Shmeliov, A.; Mourad, M.C.D.; Mandel, K.; Nicolosi, V. Structural Transformation of Layered Double Hydroxides: An In Situ TEM Analysis. *NPJ 2D Mater. Appl.* **2018**, *2*, 4. [[CrossRef](#)]
27. Kaneti, Y.V.; Salunkhe, R.R.; Wulan Septiani, N.L.; Young, C.; Jiang, X.; He, Y.-B.; Kang, Y.-M.; Sugahara, Y.; Yamauchi, Y. General Template-Free Strategy for Fabricating Mesoporous Two-Dimensional Mixed Oxide Nanosheets via Self-Deconstruction/Reconstruction of Monodispersed Metal Glycerate Nanospheres. *J. Mater. Chem. A* **2018**, *6*, 5971–5983. [[CrossRef](#)]
28. Mao, C.; Shi, Z.; Peng, J.; Ou, L.; Chen, Y.; Huang, J. Hierarchically Porous Carbonized Wood Decorated with MoNi₄-Embedded MoO₂ Nanosheets: An Efficient Electrocatalyst for Water Splitting. *Adv. Funct. Mater.* **2023**, 2308337. [[CrossRef](#)]
29. Liu, G.; Sun, Z.; Shi, X.; Wang, X.; Shao, L.; Liang, Y.; Lu, X.; Liu, J.; Guo, Z. 2D-Layer-Structure Bi to Quasi-1D-Structure NiBi₃: Structural Dimensionality Reduction to Superior Sodium and Potassium Ion Storage. *Adv. Mater.* **2023**, *35*, 2305551. [[CrossRef](#)]
30. Li, L.; Ma, P.; Hussain, S.; Jia, L.; Lin, D.; Yin, X.; Lin, Y.; Cheng, Z.; Wang, L. FeS₂/Carbon Hybrids on Carbon Cloth: A Highly Efficient and Stable Counter Electrode for Dye-Sensitized Solar Cells. *Sustain. Energy Fuels* **2019**, *3*, 1749–1756. [[CrossRef](#)]
31. He, J.; Zou, Y.; Huang, Y.; Li, C.; Liu, Y.; Zhou, L.; Dong, C.-L.; Lu, X.; Wang, S. Interlayer Ligand Engineering of β-Ni(OH)₂ for Oxygen Evolution Reaction. *Sci. China Chem.* **2020**, *63*, 1684–1693. [[CrossRef](#)]
32. Putra, R.P.; Rachman, I.B.; Horino, H.; Rzeznicka, I.I. γ-NiOOH Electrocatalyst Derived from a Nickel Dithiooxamide Chelate Polymer for Oxygen Evolution Reaction in Alkaline Solutions. *Catal. Today* **2022**, 397–399, 308–315. [[CrossRef](#)]
33. Ferreira, E.B.; Tahmasebi, S.; Jerkiewicz, G. On the Catalytic Activity and Corrosion Behavior of Polycrystalline Nickel in Alkaline Media in the Presence of Neutral and Reactive Gases. *Electrocatalysis* **2021**, *12*, 146–164. [[CrossRef](#)]
34. Wilhelm, M.; Bastos, A.; Neves, C.; Martins, R.; Tedim, J. Ni-Fe Layered Double Hydroxides for Oxygen Evolution Reaction: Impact of Ni/Fe Ratio and Crystallinity. *Mater. Des.* **2021**, *212*, 110188. [[CrossRef](#)]

35. Faid, A.Y.; Barnett, A.O.; Seland, F.; Sunde, S. Ni/NiO Nanosheets for Alkaline Hydrogen Evolution Reaction: In Situ Electrochemical-Raman Study. *Electrochim. Acta* **2020**, *361*, 137040. [[CrossRef](#)]
36. Nieuwoudt, M.K.; Comins, J.D.; Cukrowski, I. The Growth of the Passive Film on Iron in 0.05 M NaOH Studied In Situ by Raman Micro-Spectroscopy and Electrochemical Polarisation. Part I: Near-Resonance Enhancement of the Raman Spectra of Iron Oxide and Oxyhydroxide Compounds: Near Resonance Enhancement of Raman Spectra of Iron Oxides and Oxyhydroxides. *J. Raman Spectrosc.* **2011**, *42*, 1335–1339. [[CrossRef](#)]
37. Yan, P.; Liu, Q.; Zhang, H.; Qiu, L.; Wu, H.B.; Yu, X.-Y. Deeply Reconstructed Hierarchical and Defective NiOOH/FeOOH Nanoboxes with Accelerated Kinetics for the Oxygen Evolution Reaction. *J. Mater. Chem. A* **2021**, *9*, 15586–15594. [[CrossRef](#)]
38. Wu, B.; Gong, S.; Lin, Y.; Li, T.; Chen, A.; Zhao, M.; Zhang, Q.; Chen, L. A Unique NiOOH@FeOOH Heteroarchitecture for Enhanced Oxygen Evolution in Saline Water. *Adv. Mater.* **2022**, *34*, 2108619. [[CrossRef](#)]

Disclaimer/Publisher’s Note: The statements, opinions and data contained in all publications are solely those of the individual author(s) and contributor(s) and not of MDPI and/or the editor(s). MDPI and/or the editor(s) disclaim responsibility for any injury to people or property resulting from any ideas, methods, instructions or products referred to in the content.